RESEARCH ARTICLE

Investigation of a Low-Speed High-Torque-Density Direct-Drive External-Rotor PMSM for Belt Conveyor Application

YONGDA SONG, GUANGWEI LIU, (Member, IEEE), SIYANG YU, (Member, IEEE), HAO WANG, AND FENGGE ZHANG, (Member, IEEE)
School of Electrical Engineering, Shenyang University of Technology, Shenyang 110870, China
Corresponding author: Guangwei Liu (liu-guangwei@hotmail.com)

ABSTRACT Aiming at the shortcomings of complex mechanical transmission structure and low efficiency of the existing belt conveyor driven by asynchronous motor, this paper focuses on the investigation of a new type of low-speed high-torque-density direct-drive permanent magnet synchronous motor (LHDPMSM) for driving the belt conveyor. The proposed LHDPMSM utilizes external rotor structure to achieve the goal of fully direct drive of the belt conveyor. First, the topology and advantages of the straight-shape external-rotor LHDPMSM is introduced. Then the selection rules of the pole-slot combination are studied. Furthermore, an improved subdomain model is established based on the idea of segmentation for fast calculation of the no-load magnetic field of the proposed straight-shape external-rotor LHDPMSM. Moreover, the operating performance of the proposed LHDPMSM with load fluctuations was verified by FEA. In addition, an efficient cooling system based on Z-shape water channels and hollow shaft was designed, and a LPTN model was established for temperature fast calculation. Since the cooling system has a negative impact on the shaft mechanical strength, the mechanical strength of the shaft and other fragile components of the LHDPMSM was analyzed to ensure the safe operation of the motor. Finally, a prototype is manufactured and tested to validate the design concept introduced in this paper.

INDEX TERMS Low-speed high-torque-density, external rotor, PMSM, LPTN, cooling system, belt conveyor.

I. INTRODUCTION

In recent years, the application of the external-rotor permanent magnet synchronous machine (ERPMSM) has become increasingly widespread [1], [2], [3], and the research of the ERPMSM has been a hotspot. However, most of these researches focus on the electric vehicle application. The research on the low-speed high-torque-density direct-drive ERPMSM (LHDERPMSM) for belt conveyor application is extremely rare. As a modern transportation equipment, the belt conveyor is widely used in factories, ports, mining, etc. [4]. At present, most of the belt conveyors are

The associate editor coordinating the review of this manuscript and approving it for publication was Qinfen Lu.

still driven by asynchronous motor cooperates with speed reducer. Although this driving method is technically mature and robust, however, due to some inherent shortcomings of the asynchronous motor, there are still many problems have not been solved. For example, complex mechanical transmission structure (asynchronous motor + speed reducer + drive roller), loud noise, low efficiency, etc. When using the proposed LHDERPMSM to drive the belt conveyor, these problems can be resolved. The proposed LHDERPMSM not only omits the speed reducer and drive roller, but also maintains high efficiency over a wide load range.

For the investigation of the LHDERPMSM, pole-slot combination selection, no-load back electromotive force (BEMF) fast calculation, efficient cooling system design and

mechanical strength analysis are the key to improving the motor design efficiency and ensuring long-term efficient and stable operation of the motor. Some research has been conducted on the pole-slot combination of the PMSM. In [5], a novel vibration reduction method which combines the modified slot–pole combination and optimal slot opening coefficient is researched and verified. In [6], a new pole-slot combination with higher winding factor, lower total harmonics distortion (THD) of the no-load BEMF and lower cogging torque is presented based on three-slot pitch coils. In [7], the influence of slot-pole combination on torque density and flux weaking ability of the wheel-hub machine is analyzed, and the result indicates that it is best to choose a slightly smaller pole number than the slot number. In [8], for in-wheel permanent magnet vernier motors (PMVM), the influence of slot-pole combination on BEMF harmonic is researched and the PMVM with two slot pitches corporate with open-slot stator is determined as the better combination. As for the proposed LHDERPMDM, the pole-slot combination needs to meet the requirements of outputting maximum torque within a limited volume. Therefore, the above research conclusions are not fully applicable to the LHDERPMSM studied in this paper.

The no-load BEMF is an important index for LHDER-PMSM performance evaluation [9]. The value of the BEMF directly influence the power factor, efficiency, overload capability and starting performance of the motor. Furthermore, the harmonic content of the BEMF can also influence the torque ripple, vibration, noise and eddy current loss of the motor [10]. Generally, the no-load BEMF is obtained by FEA, which is time consuming. Therefore, it is of great significance to establish the no-load BEMF analytical model to improve the initial parameters design efficiency of the LHDERPMSM. The authors in [11] presents new magnetic field calculation model based on the combination of magnetic equivalent circuit and rotor magnetic potential model. In [12], the method of combining the subdomain method and the magnetic equivalent circuit method is proposed for V-shape interior PMSM magnetic field calculation. In [13], a rotor magnetic potential model which can accurately calculate the rotor surface magnetic potential distribution is proposed and applied to the spoke-type machine. At present, the subdomain model which depends on dividing the motor solution domain into several subdomains and solving the corresponding partial differential equations to obtain the magnetic field results is the most commonly used magnetic field calculation method [14], [15], [16], [17], [18]. As for the proposed LHDERPMSM, the straight-shape PM not meet the annular boundary condition of the subdomain model,therefore further research is required.

As for the ERPMSM cooling system design and mechanical strength analysis, many scholars have conducted relevant research. In [19], a high-performance cooling system based on heat pipe technology is proposed for external-rotor surface mounted PMSM. In [20], different cooling schemes include air cooling-method and water-cooling method are researched

and compared for a high-torque-density ERPMSM. In [21], the spiral waterway cooling structure is presented for an external rotor in-wheel motor. In [22], the thermal field distribution of the ERPMSM for E-bike was analyzed by the lumped thermal network and the V-shaped rotor core strength was analyzed under different speeds. For the proposed LHDERPMSM, due to the need to drive heavy load, higher requirements are placed on the cooling capacity of the motor cooling system and the mechanical strength of the important components, which requires in-depth research.
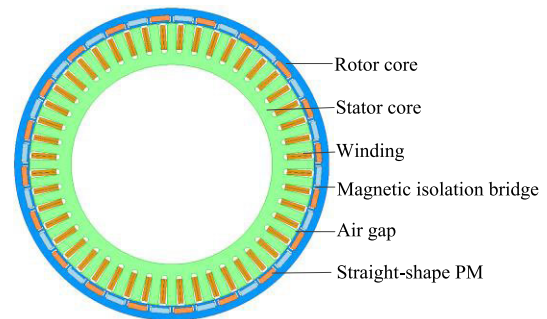

FIGURE 1. The structure of the proposed straight-shape LHDERPMSM.

II. STRAIGHT-SHAPE LHDERPMSM TOPOLOGY
Fig. 1 shows the topology of the proposed straight-shape LHDERPMSM. The stator slot is arranged on the outside of the stator, and the straight-shape PM is embedded in the rotor part close to the stator. The thin bridge is designed to reduce the flux leakage and improve the output torque, while keeping the rotor mechanically rigid. In contrast with the traditional surface-mounted ERPMSM, the proposed LHDERPMSM has some unique advantage. First, when the PM is surrounded by the magnetic isolation bridge, the risk of PM falling off or shifting can be eliminated. Furthermore, the PM can also be protected safely from damage caused by assembly, bearing damage, eccentricity, etc. Second, the PM of the proposed LHDERPMSM adopts cuboid structure, this structure not only saves PM materials, but also is easy to process. Third, the PM of the surface-mounted PMSM (SPMSM) needs to be firmly fixed to the rotor core through trapezoidal aluminum pressure plates and bolts, as shown in Fig.2. The existence of the pressure plates and bolts will greatly hinder the improvement of the pole arc coefficient of the PM, thereby affecting the improvement of the LHDERPMSM torque density. Based on the above advantages, the proposed straight-shape PM structure was determined as the most suitable topology for LHDERPMSM.

III. POLE-SLOT COMBINATION SELECTION
The proposed LHDERPMSM needs to output as much torque as possible within a limited motor volume, which will lead to a contradiction between the volume and the torque output capability. According to (1) and (2), when the power is constant, the output torque is inversely proportional to
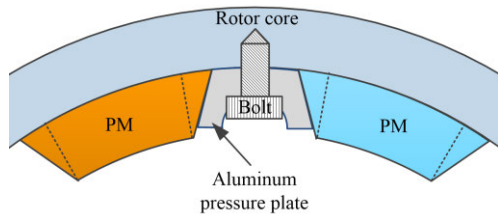
FIGURE 2. The schematic diagram of the PM installation method for traditional SPMSM.

FIGURE 3. The reduction of 5th and 7th harmonics by short-pitch winding.

the speed. Therefore, the lower the speed, the greater the output torque. Furthermore, the speed is inversely proportional to the pole pairs number, so the larger pole pairs number, the lower the rated speed of the motor. Therefore, in order to maximize the output torque capability of the LHDERPMSM, the multiple-pole design of the motor is required. As for the traditional integer slot winding (ISW), the achievement of multiple-pole design must correspond to the multiple-stator slot number. However, if the slot number increases significantly, it will not only cause the stator teeth to be too narrow, leading to insufficient mechanical strength or magnetic saturation, but also reduce the installation space of the winding due to the increase in the use of the insulation materials, thereby reducing the torque density of the motor. Contrary to ISW, fractional slot winding (PFSW) means that the multipole design of the LHDERPMSM can be realized with less stator slots.

$$T = \frac{60P}{2\pi n} \quad (1)$$

$$n = \frac{60f}{p} \quad (2)$$

where, T denotes the output torque. P denotes the motor rated power. n denotes the motor speed. f denotes the frequency. p denotes the pole pairs number.

The existence of the harmonic will cause an increase in torque ripple and lead to hazards such as vibration and noise. Therefore, the harmonic content is an important factor in evaluating whether the pole-slot combination is optimal. Due to the use of star connection at the end of the three-phase winding, the third-order harmonic can be eliminated. Therefore, the focus of the pole-slot combination selection is to reduce the fifth-order (5th) and seventh-order (7th) harmonic content. Fig.3 shows the schematic diagram of using short-pitch winding to reduce 5th and 7th harmonics. To simultaneously reduce 5th and 7th harmonics, the pitch y_1 should be determined as the five sixths of the polar pitch, as shown in (3).

$$y_1 = \frac{5}{6}\tau = \frac{5}{6} \times \frac{Z}{2p} = \frac{5}{6}mq \quad (3)$$

where, τ denotes the polar pitch. Z denotes the stator slot number. m denotes the phase number, $m = 3$. q denotes the stator slots per pole per phase.
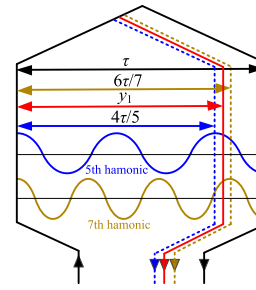
According to the definition of pitch, the y_1 can only be set as an integer. Therefore, in order to make full use of the harmonic reduction ability of the short-pitch winding of the proposed LHDERPMSM, the value of q shown in (3) should be determined as $0.4s$ ($s = 1,2\ldots$). When the s is determined as 1, the q equals 0.4 and y_1 equals 1. At this time, the PFSW becomes the FSCW. The advantages of adopted FSCW are shown as follows.

1) The end of the FSCW does not need to span several slots, which significantly shortens the length of the winding end and the prototype.

2) There is no overlap between the ends of the adjacent coils, which is extremely easy for coil inserting

3) The PFSW means single tooth wound structure, which allows more copper to be placed in the slot. A higher copper filling factor plays a key role in improving the torque density of the LHDERPMSM.

TABLE 1. Major parameters of the proposed LHDERPMSM.

Parameters	Symbols	Parameter
Rotor type	-	External
Rated power (kW)	P	93
Rated voltage (V)	U_N	1140
Stator slot	Z	48
Frequency (Hz)	f	22.67
Rotor OD (mm)	R_r	755
Pole number	p	40
Rated output torque (kN·m)	T_N	13.06
Overload multiple	s	1.8
Permanent magnet	-	N38SH

When q is determined as 0.4, according to (3), the relationship between the stator slot number and pole number can be expressed as (4). Therefore, the pole-slot combination of the unit motor is determined as 10-12. Then, the pole-slot combination of the whole LHDERPMSM is determined as $10s$-$12s$ ($s = 1, 2, 3\ldots$). As for the LHDERPMSM researched in this paper, the outer diameter of the motor is limited by the actual working conditions. Therefore, too much slot number will lead to narrow stator teeth width and reduce the mechanical strength of the stator. Finally, the pole-slot combination of the LHDERPMSM proposed in this paper is determined as 40-48. Table 1 presents the major parameters

and symbols of the proposed LHDERPMSM.

$$Z/2p = 1.2 \tag{4}$$
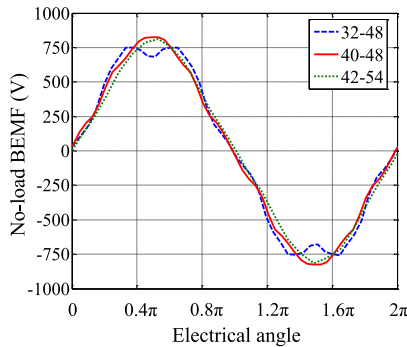
FIGURE 4. The comparison of the BEMF waveforms of the LHDERPMSM with different pole-slot combinations.

In order to verify the superiority of the pole-slot combination of 40-48. Two LHDERPMSM have been redesigned with pole-slot combination of 32-48 and 42-54, respectively. Fig.4 shows the BEMF of the LHDERPMSM with these three different pole-slot combinations, and Table 2 compares the total harmonic distortion (THD) of the corresponding BEMF. It can be found from Fig.4 and TABLE 2 that the distortion of the 32-48 is the most severe. Furthermore, the distortion degree of the BEMF of 40-48 and 42-54 is relatively similar. By comparing the THD, it can be found that the THD of 40-48 is lower, indicating a stronger ability to suppress harmonics. Therefore, for the LHDERPMSM studied in this paper, 40-48 is the most suitable pole-slot combination.

**TABLE 2.** THD of no-load BEMF with different pole-slot combinations.

Combination	40 pole-48 slot	32 pole-48 slot	42 pole-54 slot
THD	8.04%	10.30%	8.6%

IV. NO-LOAD BEMF ANALYSIS

The rapid acquisition of the no-load BEMF is important for improving the design efficiency of the initial parameters of the LHDERPMSM. Although some initial work is required to establish the no-load BEMF analytical model, they are very time-consuming compared with FEA. Due to the non-circular arc shape of the proposed straight-shape PM of the LHDERPMSM, the PM not meet the boundary condition of the traditional subdomain model. Therefore, the traditional subdomain model cannot be used directly. To solve this problem, the improved subdomain model based on segmentation idea is presented. In order to simplify the subdomain model, some assumptions are made as follow. 1) The PM is fully magnetized in the radial direction. 2) The diameter of the ERPMSM is larger than the PM thickness,

therefore, it is assumed that the two short edges of the PM are along the radial direction.

Based on segmentation idea, the PM is segmented into N pieces along the radial direction. When N is infinite, the outer and inner edges of the small PM block are approximately concentric with the rotor. Then the magnetic field corresponding to each small PM block can be solved by traditional subdomain model. After solving the magnetic field corresponding to each small PM block, the complete magnetic field of the LHDERPMSM can be obtained by superposition along circumferential position.
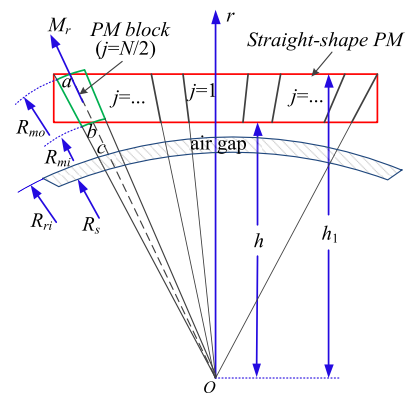
FIGURE 5. The simplified diagram of the divided permanent magnet.

The simplified diagram of the segmentation of one PM is shown as Fig. 5. In Fig. 5, the red rectangle represents the whole PM. The small PM block obtained by segmentation is shown as the green part. The whole PM is divided into two symmetrical parts along the r-axis. Furthermore, the left part is divided into $N/2$ pieces, as well as the right part. The central angle of each part can be expressed as (5).

$$\theta = \frac{\pi \alpha_p}{pN} \tag{5}$$

where, α_p denotes the effective pole arc coefficient. R_{mo} and R_{mi} denotes the outer radius and inner radius of the PM block, respectively. The expressions of R_{mo} and R_{mi} can be expressed as (6)-(7).

$$R_{mi} = \frac{h}{\cos\left[\pi \alpha_p(j - 0.5)/(pN)\right]} \tag{6}$$

$$R_{mo} = \frac{h_1}{\cos\left[\pi \alpha_p(j - 0.5)/(pN)\right]} \tag{7}$$

where, h denotes the distance between the stator center to the rectangular PM inner edge, h_1 denotes the distance between the stator center to the rectangular PM outer edge, j denotes the serial number of the PM block. When the central angle θ is determined, the angle range of each small PM block can also be determined. Therefore, the magnetization of a pair of permanent magnets can be expressed by a piecewise function,

as shown below.

$$\left.\begin{array}{l} M_r = 0 \\ M_\theta = 0 \end{array}\right\} \qquad -\alpha_p \frac{\pi}{2p} < \theta < -\frac{\pi \alpha_p}{pN}j \qquad (8)$$

$$\left.\begin{array}{l} M_r = B_r / \mu_0 \\ M_\theta = 0 \end{array}\right\} \qquad -\frac{\pi \alpha_p}{pN}j < \theta < -\frac{\pi \alpha_p}{pN}(j-1) \qquad (9)$$

$$\left.\begin{array}{l} M_r = 0 \\ M_\theta = 0 \end{array}\right\} \qquad -\frac{\pi \alpha_p}{pN}(j-1) < \theta < \frac{\pi}{p}\left(1 - \frac{\alpha_p}{N}j\right) \qquad (10)$$

$$\left.\begin{array}{l} M_r = -B_r / \mu_0 \\ M_\theta = 0 \end{array}\right\} \qquad \frac{\pi}{p}\left(1 - \frac{\alpha_p}{N}j\right) < \theta < \frac{\pi}{p} - \frac{\pi \alpha_p}{pN}(1-j) \qquad (11)$$

$$\left.\begin{array}{l} M_r = 0 \\ M_\theta = 0 \end{array}\right\} \qquad \frac{\pi}{p} - \frac{\pi \alpha_p}{pN}(1-j) < \theta < (4-\alpha_p)\frac{\pi}{2p} \qquad (12)$$

where, M_r denotes the radial magnetization component, M_θ denotes the tangential magnetization component, B_r denotes the residual magnetic flux density, μ_0 denotes the vacuum permeability. Through Fourier analysis of (8)-(12), the radial magnetization can be expressed as (13)-(14).

$$M_r = \sum_{n=1,3,5\ldots}^{\infty} M_{rn} \cos(np\theta) \qquad (13)$$

$$M_{rn} = \frac{2 B_r}{n\pi \mu_0}\left[\sin\left(\frac{n\pi \alpha_p}{N}j\right) - \sin\left(\frac{n\pi \alpha_p}{N}(j-1)\right)\right] \qquad (14)$$

Secondly, for the PM block that $j = N/2$, the equivalent outer and inner radius of the PM are equivalent as follows.

$$R_{mij} = R_{mi} - l_{bc} \qquad (15)$$

$$R_{moj} = R_{mo} - l_{bc} \qquad (16)$$

where, l_{bc} denotes the length between point b and point c, as shown in Fig. 3. It should be notes that the length of l_{bc} corresponding to each permanent magnet block is different. In addition, the influence of the magnetic isolation bridge on flux leakage will be described by the leakage coefficient σ_0. Therefore, the air gap flux density can be expressed as (17)-(19). The expression of the no-load BEMF can be expressed as (20).

$$B_r(\theta)$$
$$= \sum_{j=1,2,3\ldots}^{N/2} \sum_{n=1,3,5\ldots}^{\infty} \frac{2}{\sigma_0} f_{Br}(r) \cdot k_B(n) \cdot \cos(np\theta) \qquad (17)$$

$$f_{Br}(r)$$
$$= \left(\frac{r}{R_{mij}}\right)^{np-1} + \left(\frac{R_s}{R_{mij}}\right)^{np-1}\left(\frac{R_s}{r}\right)^{np+1} \qquad (18)$$

$$K_B(n)$$
$$= \frac{-\mu_0 M_r}{\mu_r} \frac{np}{(np)^2 - 1}$$
$$\cdot \frac{(np-1)(R_{mij}/R_{moj})^{2np} + 2(R_{mij}/R_{moj})^{np-1} - (np+1)}{\frac{\mu_r+1}{\mu_r}\left[1 - \left(\frac{R_s}{R_{moj}}\right)^{2np}\right] - \frac{\mu_r-1}{\mu_r}\left[\left(\frac{R_s}{R_{mij}}\right)^{2np} - \left(\frac{R_{mij}}{R_{moj}}\right)^{2np}\right]} \qquad (19)$$

EMF

$$= \frac{d\left(N_1 R_s L_{ef} \int_{\theta-\theta_c}^{\theta+\theta_c} B_r(\theta) d\theta\right)}{dt} = -2 N_1 R_s L_{ef} \omega_r \frac{2}{\sigma_0}$$
$$\cdot \sum_{j=1,2,3}^{N/2} \sum_{n=1,3,5}^{\infty} K_B(n) f_{Br}(r) \sin(np\theta) \sin\left(\frac{np\,\theta_c}{2}\right) \qquad (20)$$

where, μ_r denotes the relative permeability. R_s denotes the stator outer radius. N_1 denotes the number of series turns per phase. L_{ef} denotes the stator core length. ω_r denotes angular velocity. θ_c denotes coil pitch.

In order to test the accuracy of the above improved subdomain model for no-load BEMF calculation of the proposed straight-shape LHDERPMSM. The FEA model of the LHDERPMSM is established and the no-load BEMF is obtained. The simulation and analytical results of the no-load BEMF are shown in Fig. 6. It can be found that these two waveforms are in good agreement. Therefore, the proposed analytical model is reliable for the no-load BEMF calculation of the proposed straight-shape LHDERPMSM.
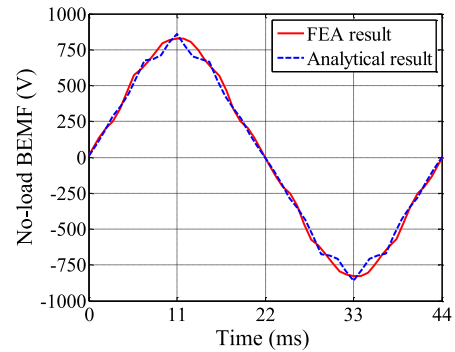

FIGURE 6. Comparison of the no-load BEMF obtained by FEA and analytical method.

V. LHDERPMSM PERFORMANCE EVALUATION

As for the traditional asynchronous motor, the efficiency of the motor is greatly influenced by the load ratio, which limits the energy-saving effect of the motor. As for the belt conveyor proposed in this paper, the load ratio ranging from 0.3 to 1. Furthermore, the expression of the electromagnetic torque of the LHDERPMSM is expressed as (21). Therefore, with the load ratio increase, a larger q-axis current is required. The effect of q-axis and d-axis current on output torque is shown in Fig. 7. It should be emphasized that when the magnetic density exceeds 2.0T, the silicon steel sheet enters the magnetic saturation zone.

$$T_e = 3/2 \cdot p \, \psi_f \, i_q \qquad (21)$$

where, ψ_f denotes PM magnetic linkage, i_q denotes the q-axis current.

It can be seen that when the q-axis current excitation is used along, the flux lines coupling stator core and the rotor core are abundant, which is beneficial to improve the
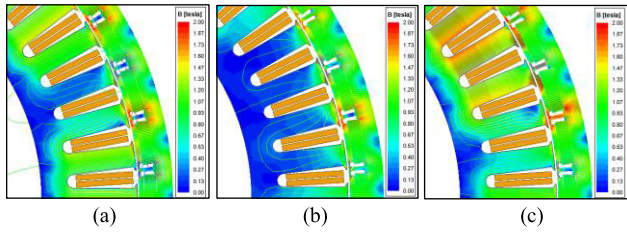
FIGURE 7. Effect of d-axis and q-axis current excitation on flux distribution. (a) No load condition. (b) Full load *d*-axis current excitation. (c) Full load *q*-axis current excitation.
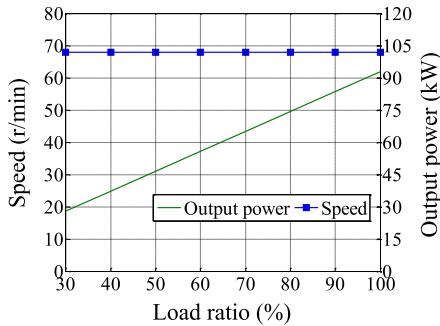

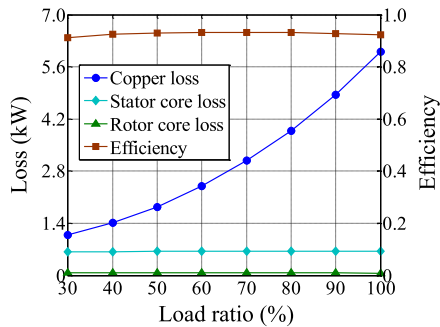**FIGURE 8.** Speed-load ratio-output power characteristics of the LHDERPMSM.

FIGURE 9. Loss-load ratio-efficiency characteristics of the LHDERPMSM.

torque output capacity of the LHDERPMSM. Contrary to the effect of *q*-axis current, *d*-axis current will generate a magnetic field opposite to the excitation field, so as to broaden the speed range of the LHDERPMSM. Since the proposed LHDERPMSM is used for belt conveyor, the speed of the motor is usually maintained at the rated speed and does not change with the change of load. Fig. 8 denotes the speed-load ratio-output power characteristics of the proposed LHDERPMSM, and Fig. 9 denotes the loss-load ratio-efficiency characteristics of the LHDERPMSM obtained by FEA. Compared with traditional asynchronous motor, the efficiency of the proposed LHDERPMSM can still be maintained at a high level during a wide load range, which is one of the advantages of using LHDERPMSM to drive the belt conveyor. Since the frequency of the LHDERPMSM is low, the stator core loss and rotor core loss are low. For copper loss, the proposed LHDERPMSM needs to drive heavy load,

so the winding current is large, which leads to large copper loss of the motor. High copper loss leads to high winding temperature, which has a bad effect on slot insulation and PM. Therefore, the temperature field analysis of LHDERPMSM is crucial.
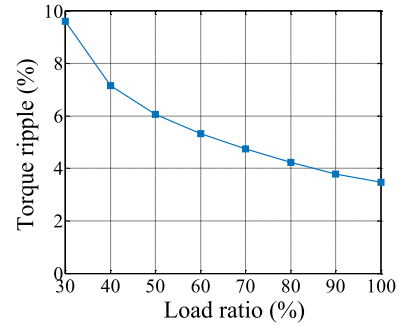

FIGURE 10. Torque ripple-load ratio characteristics of the ERPMSM.

Fig. 10 denotes the load ratio-torque ripple characteristics of the LHDERPMSM. It can be seen that the torque ripple decreases with the increase of the load. This is because the saturation of the stator teeth increases with the torque increase, resulting in small variation of the reluctance [22]. The overall torque fluctuation of the ERPMSM is at a reasonable level.

VI. THERMAL ANALYSIS

As described in section V, due to high copper loss, the LHDERMSM proposed in this paper has a higher risk of PM high-temperature demagnetization and insulation fatigue. Furthermore, the poor heat dissipation condition of the LHDERPMSM further exacerbated these risks. First, the stator of the LHDERPMSM is surrounded by the external rotor, which is not conducive to the winding heat dissipation. Second, the external surface of the proposed LHDERPMSM is covered by a thick rubber layer to improve the friction. The lower thermal conductivity of the rubber further inhibits the heat dissipation of the PM. Third, the proposed LHDERPMSM is an explosion-proof motor, and the air gap is sealed, which is not conducive to heat dissipation. Therefore, the design of an efficient cooling system and thermal field analysis are the major factors affecting the service life of the LHDERPMSM for belt conveyor application.

At present, water cooling is the most direct and effective way to reduce the motor temperature [23], [24]. Due to the external rotor structure of the proposed LHDERPMSM, the inlet and outlet of cooling water cannot be directly installed on the shell like the outer stator PMSM. In order to realize the water cooling of the proposed LHDERPMSM, the structure of leading out the water inlet and outlet through the shaft is presented in this paper. Generally, spiral water channel is the most commonly used motor cooling structure due to low water flow resistance. However, when the spiral water channel is adopted for the proposed LHDERPMSM, the water outlet and water inlet must be at both ends of the

stator respectively. Therefore, water holes need to be drilled at both ends of the shaft, one as the water inlet and the other as the water outlet. This cooling structure design will not affect the cooling capacity of the LHDERPMSM, but will affect the extraction of the three-phase winding. Because the leading out of the three-phase winding must also pass through the shaft. Therefore, according to the structure characteristics of the proposed LHDERPMSM, the Z-shape water channel is adopted.
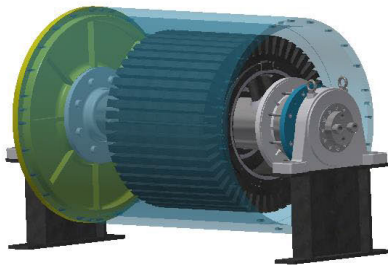

FIGURE 11. The overall structure of the proposed LHDERPMSM.
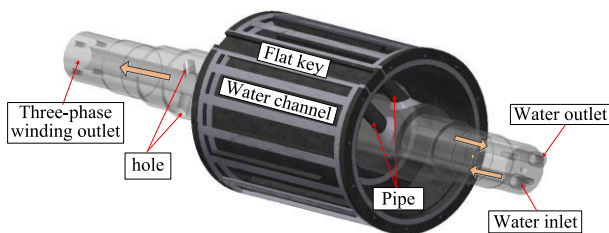

FIGURE 12. The water-cooling system structure of the proposed LHDERPMSM.

Fig. 11 shows the schematic diagram of the whole LHDERPMSM structure. The detailed structure of the water-cooling system and the hollow shaft is shown in Figure 12. It can be seen from Fig. 12 that two holes are drilled axially on the one side of the shaft as the water inlet and outlet. Furthermore, two inclined steel pipes are used to connect the water channel in shaft and the Z-shaped water channel in the stator support. In addition, the hole on the other side of the shaft serves as the outlet of the three-phase winding.

Some detailed parameters of the water-cooling structure of the proposed LHDERPMSM are shown in Table 3. Due to the need to open eight holes in the axial and radial direction of the shaft to realize the design of water-cooling structure and the extraction of the winding, this will have a negative impact on the mechanical strength of the shaft. Therefore, the verification of the shaft strength is crucial. The analysis of the mechanical strength of the shaft and some major components will be presented in section VII.

The CFD is often used for thermal calculation of the motor. In order to solve the problem of complex modelling process and long calculation time of the CFD analysis of the proposed LHDERPMSM caused by complex motor structure and

TABLE 3. Detailed parameters of the water-cooling system.

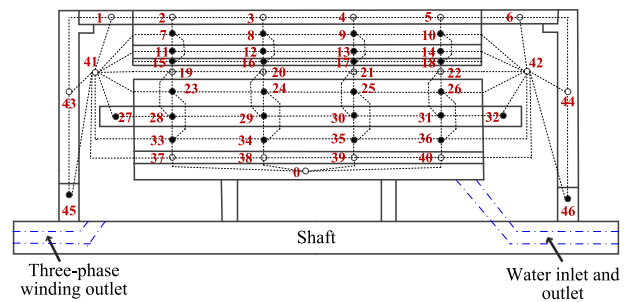| Parameter	Value
Water cooling channel width (mm)	56
Water cooling channel height (mm)	15
Number of water-cooling-channel	16
Diameter of water inlet and outlet in shaft (mm)	30
Inlet and outlet pipe inner diameter (mm)	30
Flat key occupied width (mm)	60
Water velocity (m/s)	0.6

FIGURE 13. Node connections of the LPTN model of the proposed LHDERPMSM.

large volume, the corresponding lumped parameter thermal network (LPTN) model was established. Due to the heat insulation effect of the rubber and belt, the convective effect on the outer surface of the rotor is ignored. Figure 13 shows the node connection of the LPTN model.

Node 0 denotes the cooling water channel; Nodes1-6 denotes the rotor steel rings; Nodes7-10 denotes rotor yoke; Nodes 11-14 denotes PM; Nodes 15-18 denotes the silicon steel sheet circular ring between the PM and air gap; Nodes 19-22 denotes the air gap; Nodes 23-26 denotes the stator teeth; Nodes 27-32 denotes the stator winding; Nodes 33-36 denotes the stator yoke; Nodes 37-40 denotes the water-cooling plate; Nodes 41-42 denotes the air cavity; Nodes 43-44 denotes the end cap; Nodes 45-46 denotes the bearing. In addition, the relevant thermal resistance calculation can refer to [25].
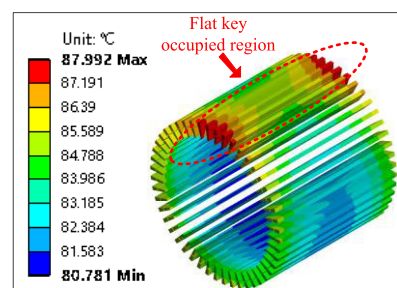

FIGURE 14. The diagram of the winding temperature distribution.

In this paper, the CFD is also conducted to verify the accuracy of the LPTN model. The temperature distribution of the stator winding and PM are shown in Fig. 14 and Fig.15, respectively. Due to the difficulty of heat dissipation at the
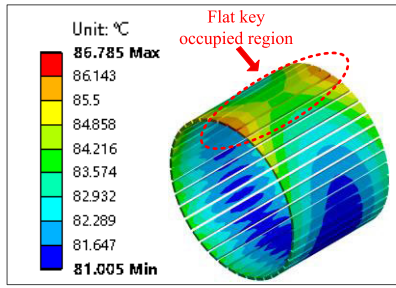
FIGURE 15. The diagram of the PM temperature distribution.

TABLE 4. The comparison of the PM and winding temperature calculated by LPTN and CFD.

Component	LPTN (°C)	CFD (°C)	Error (%)
PM	81.45	86.79	6.15%
Winding	83.63	87.99	4.96%

winding end, the temperature of the winding end is greater than that in the middle. The maximum temperature of the winding is about 87.992°. Furthermore, the maximum temperature of the PM is about 86.785°. In addition, Table 4 compares the winding and PM max temperature calculated by LPTN model and CFD.

It can be seen from TABLE 4 that there is an error between the LPTN results and the CFD results. As for the CFD results, since the stator support and the stator core need to be fixed by a flat key, there is no water-cooling channel installed on this part of the stator support, which leads to a high temperature rise of the PM and winding of the corresponding region. However, as for the LPTN model, the existence of the flat key was ignored and it was assumed that the water channels were uniformly distributed within the stator support. Therefore, the temperature results calculated by LPTN are small. Due to the small error of the LPTN and CFD results, it is reliable to quickly obtain the temperature of the proposed LHDERPMSM through the established LPTN model. In summary, both simulation and calculation results indicate that the temperature of the winding and PM is controlled within a safe range by using the proposed water-cooling structure, which verifies the effectiveness of the proposed water-cooling system.

VII. MECHANICAL STRENGTH ANALYSIS

The straight-shape rotor part is the major torque output components of the proposed LHDERPMSM. Many trade-offs exist between the electromagnetic performance and the mechanical strength of the rotor structure of the proposed LHDERPMSM. For instance, by reducing the thickness of the magnetic isolation bridge, the flux leakage of the rotor can be reduced and the electromagnetic performance of the motor can be improved, but the mechanical strength of the rotor will be reduced. Therefore, it is necessary to verify the mechanical strength of the proposed rotor structure while ensuring its excellent electromagnetic performance.

Furthermore, as shown in Fig.12, since multiple holes need to be drilled in the shaft along axial and radial direction, the interior of the shaft is no longer solid, but a complex hollow structure. The large output torque reaction force and the gravity of the LHDERPMSM put forward high requirements on the mechanical strength of the shaft. Therefore, the analysis of the shaft strength is also a top priority. Ansys is regularly used to calculate the mechanical deformation of the complex mechanical structure, and the results are close to the actual situation. When the mechanical strength of the rotor and shaft is analyzed by Ansys, the mechanical parameters of the material are shown as follows.

1) The rotor core is made of silicon steel sheet DW465-50. The mechanical characteristics of DW465-50 are shown as follow: density $\rho = 7650$kg/m3, Young's modulus E $= 2.05 \times 105$ MPa, Poisson's Ratio $\gamma = 0.27$, yield strength $[\sigma s] = 390$MPa, and ultimate tensile strength $[\sigma t] = 500$MPa.

2) The shaft is made of 40Cr. The mechanical characteristics of the 40Cr are shown as follows: density $\rho = 7850$kg/m3, Young's modulus E $= 2.11 \times 105$ MPa, Poisson's Ratio $\gamma = 0.29$, yield strength $[\sigma s] = 785$MPa, and ultimate tensile strength $[\sigma t] = 980$MPa.

TABLE 5. Mechanical stress and displacement analysis of the rotor core.

Torque	Displacement (m)	Von Mises Stress (Pa)
13.06 kN·m	Max:2.893e-5	Max:4.720e7
23.51 kN·m	Max:5.207e-5	Max:8.496e7

Table 5 shows the contour plots of the Von Mises stress distribution (result unit: Pa) and Displacements (result unit: m) results of the rotor core under rated load condition and short-term maximum overload condition. It can be seen that under rated load condition, the maximum displacement occurs at the magnetic isolation bridge of the central part of the core, about 0.0289mm. Furthermore, the max stress occurs at the root of the magnetic isolation bridge, about 47.2MPa. When under overload condition, the max displacement and stress are about 0.0521mm and 84.96 MPa, and the occurrence position is the same as that under rated load condition. Both stress and displacement are within the safety range.
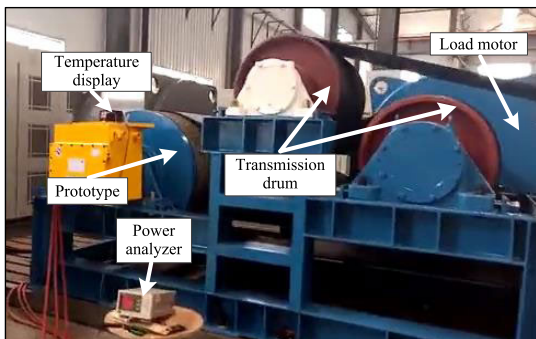
Table 6 shows the contour plots of the Von Mises stress distribution (result unit: Pa) and Displacements (result unit: m) results of the shaft under rated load condition and short-term maximum overload condition. It can be seen that under rated load condition, the max displacement occurs at the contact position between the stator core support and shaft,

TABLE 6. Mechanical stress and displacement analysis of the shaft.

Torque	Displacement (m)	Von Mises Stress (Pa)
13.06 kN·m	Max: 5.675e-5	Max:1.359e8
23.51 kN·m	Max:9.548e-5	Max:2.435e8

FIGURE 17. The experimental waveform of the no-load BEMF of the prototype.

TABLE 7. RMS value and THD of the no-load BEMF.

Type	BEMF (V)	BEMF Error (%)	THD(%)
Analytical result	533.9	2.72	8.20
FEA result	552.4	0.66	8.04
Experiment result	548.8	-----	4.03

about 0.057mm. Furthermore, the maximum stress occurs at the shaft near the motor support, about 135.9MPa. When under maximum overload condition, the max displacement and stress are about 0.095mm and 243MPa, and the occurrence position is the same as that under rated load condition. Both stress and displacement are within the safety range. Therefore, through reasonable parameter design, the mechanical strength of the straight-shape rotor structure and the hollow shaft proposed in this paper for LHDERPMSM can be guaranteed.
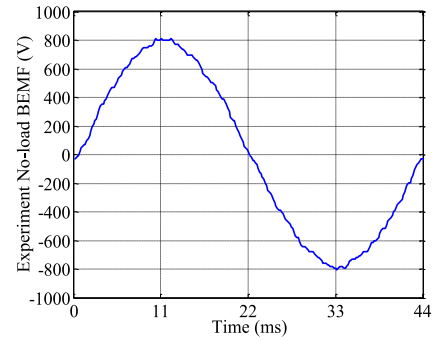
improved subdomain model are close to the experimental result, proving the accuracy of the model.

FIGURE 16. The experimental platform of the prototype LHDPMSM.

FIGURE 18. The tested winding temperature of the prototype LHDERPMSM.

VIII. EXPERIMENT VALIDATION
In this paper, the prototype LHDERPMSM has been manufactured and tested to validate the design concept introduced in this paper. The prototype LHDERPMSM testing platform is shown in Fig.16. An inner rotor PMSM is served as the load motor, and the connection with the prototype is realized by the turnabout drum and belt.

Fig. 17 shows the measured no-load BEMF of the prototype LHDERPMSM. The root mean square (rms) value and the THD of the no-load BEMF obtained by analytical method, FEA method and experiment are compared in Table 7. It can be seen that the rms value and THD obtained by the proposed
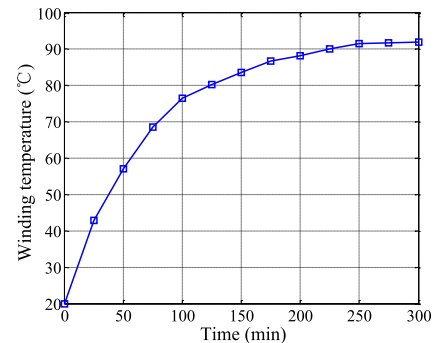
In order to measure the winding temperature, the Pt100 is placed in advance in the stator slot and close to the flat key occupied region. Record temperature data every 25 minutes. The temperature variation trend of the stator winding is shown in Figure 18. It can be seen from Fig.18 that the maximum winding temperature is about 91.9°, which meets the LHDERPMSM initial design requirements and demonstrates the effectiveness of the proposed cooling system.

TABLE 8 compares the winding temperatures obtained by CFD, LPTN and the experiment. The error between the results of CFD, LPTN and the experimental result is very small, which verifies the reliability of the LPTN model and CFD model.

Figure 19 compares the efficiency of the prototype LHDERPMSM under different load condition. It can be seen from Figure 19 that although the load has changes, the efficiency of the prototype has always remained at a high level.

TABLE 8. Comparison of the winding temperature of the LHDERPMSM.

Method	CFD	LPTN	Experiment	Error (%)
Temperature (°C)	87.99	-	91.9	4.25
Temperature (°C)	-	83.63	91.9	9.00
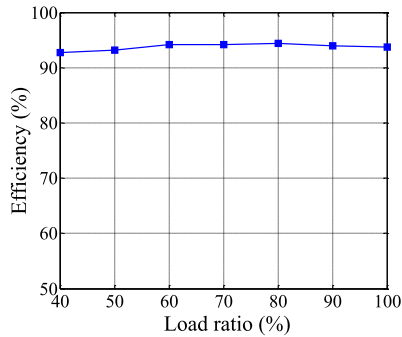
FIGURE 19. The tested efficiency of the prototype LHDERPMSM under different load condition.

This advantage is not possessed by asynchronous motors. Therefore, replacing the original asynchronous motor with LHDERPMSM is beneficial for improving the energy-saving performance of the belt conveyor.

In addition, during the long-term full load experiment process, the prototype operated stably without any abnormal phenomenon such as chamber sweeping or sudden increase of electromagnetic noise, which verified the mechanical strength of the straight-shape rotor structure and the hollow shaft.

IX. CONCLUSION

In this paper, in order to improve the operating performance of the traditional belt conveyor, a kind of LHDERPMSM for driving belt conveyor is introduced. The full paper provides a detailed study of all key issues in the design process of this type of motor. First, the selection rules for the pole-slot combination were determined and validated. Then, an improved subdomain model based on segmentation idea is proposed for fast calculation of the no-load magnetic field. In order to intuitively reflect the energy-saving advantages of the proposed LHDERPMSM, the efficiency of the motor under different load ratio is analyzed by FEA. Furthermore, an inner-stator water cooling structure is proposed based on Z-shaped water channel and hollow shaft for LHDERPMSM cooling enhancement, and a corresponding LPTN model was established to achieve the goal of fast temperature calculation. Moreover, the mechanical strength of the main components such as straight-shape external rotor core and hollow shaft was verified under rated load condition and maximum overload condition to guarantee the safe operation of the LHDERPMSM. Finally, a prototype has been manufactured and tested to validate the design concept proposed in this paper. The high degree of the coincidence between the experimental results and the theoretical results verifies the accuracy of the theory proposed in this paper.

REFERENCES

[1] R. Nasiri-Zarandi, A. Karami-Shahnani, M. S. Toulabi, and A. Tessarolo, "Design and experimental performance assessment of an outer rotor PM-assisted SynRM for the electric bike propulsion," *IEEE Trans. Transport. Electrific.*, vol. 9, no. 1, pp. 727–736, Mar. 2023.

[2] Y. Yang, M. M. Rahman, T. Lambert, B. Bilgin, and A. Emadi, "Development of an external rotor V-shape permanent magnet machine for E-bike application," *IEEE Trans. Energy Convers.*, vol. 33, no. 4, pp. 1650–1658, Dec. 2018.

[3] F. Lin, S. Zuo, W. Deng, and S. Wu, "Modeling and analysis of acoustic noise in external rotor in-wheel motor considering Doppler effect," *IEEE Trans. Ind. Electron.*, vol. 65, no. 6, pp. 4524–4533, Jun. 2018.

[4] M. Liu, Q. Zhu, Y. Yin, Y. Fan, Z. Su, and S. Zhang, "Damage detection method of mining conveyor belt based on deep learning," *IEEE Sensors J.*, vol. 22, no. 11, pp. 10870–10879, Jun. 2022.

[5] S. Zhu, W. Zhao, J. Ji, G. Liu, and C. H. T. Lee, "Design to reduce modulated vibration in fractional-slot concentrated-windings PM machines considering slot–pole combination," *IEEE Trans. Transport. Electrific.*, vol. 9, no. 1, pp. 575–585, Mar. 2023.

[6] P. Jalali, S. T. Boroujeni, and J. Khoshtarash, "Expansion of the feasible slot/pole combinations in the fractional slot PM machines by applying three-slot pitch coils," *IEEE Trans. Energy Convers.*, vol. 34, no. 2, pp. 993–999, Jun. 2019.

[7] Z. Zhu, Y. Huang, J. Dong, and F. Peng, "Investigation study of the influence of pole numbers on torque density and flux-weakening ability of fractional slot concentrated winding wheel-hub machines," *IEEE Access*, vol. 7, pp. 84918–84928, 2019.

[8] Y. Yu, Y. Pei, F. Chai, and M. Doppelbauer, "Analysis of back EMF harmonics influenced by slot–pole combinations in permanent magnet Vernier in-wheel motors," *IEEE Trans. Ind. Electron.*, vol. 70, no. 5, pp. 4461–4471, May 2023.

[9] B. Basnet, A. M. Aljehaimi, and P. Pillay, "Back-EMF analysis of a variable flux machine for different magnetization states," *IEEE Trans. Ind. Electron.*, vol. 68, no. 10, pp. 9125–9135, Oct. 2021.

[10] X. Ren, D. Li, R. Qu, and T. Pei, "Back EMF harmonic analysis of permanent magnet magnetic geared machine," *IEEE Trans. Ind. Electron.*, vol. 67, no. 8, pp. 6248–6258, Aug. 2020.

[11] S. Wu, T. Shi, L. Guo, H. Wang, and C. Xia, "Accurate analytical method for magnetic field calculation of interior PM motors," *IEEE Trans. Energy Convers.*, vol. 36, no. 1, pp. 325–337, Mar. 2021.

[12] Y. An, C. Ma, N. Zhang, Y. Guo, M. Degano, C. Gerada, Q. Li, and S. Zhou, "Open-circuit air-gap magnetic field calculation of interior permanent magnet synchronous motor with V-shaped segmented skewed poles using hybrid analytical method," *IEEE Trans. Magn.*, vol. 57, no. 12, pp. 1–9, Dec. 2021.

[13] S. Wu, L. Guo, H. Wang, Z. Wang, Z. Song, and T. Shi, "Analytical calculation for magnetic field in spoke-type permanent magnet machines based on a rotor magnetic potential model," *IEEE Trans. Magn.*, vol. 58, no. 2, pp. 1–5, Feb. 2022.

[14] C. Ma, C. Chen, Q. Li, H. Gao, Q. Kang, J. Fang, H. Cui, K. Teng, and X. Lv, "Analytical calculation of no-load magnetic field of external rotor permanent magnet brushless direct current motor used as in-wheel motor of electric vehicle," *IEEE Trans. Magn.*, vol. 54, no. 4, pp. 1–6, Apr. 2018.

[15] X. Zhang, P. Fu, Y. Ma, C. Zhang, and L. Li, "No-load iron loss model for a fractional-slot surface-mounted permanent magnet motor based on magnetic field analytical calculation," *Chin. J. Electr. Eng.*, vol. 4, no. 4, pp. 71–79, Dec. 2018.

[16] P. Liang, Y. Tang, F. Chai, K. Shen, and W. Liu, "Calculation of the iron losses in a spoke-type permanent magnet synchronous in-wheel motor for electric vehicles by utilizing the Bertotti model," *IEEE Trans. Magn.*, vol. 55, no. 7, pp. 1–7, Jul. 2019.

[17] J. Yang, J. Chen, G. Yang, S. Zhao, and C. Zhang, "Accurate calculation of magnetic field of same-pole and same-slot surface-mounted three-phase permanent magnet synchronous motor," *IEEE Trans. Magn.*, vol. 58, no. 8, pp. 1–10, Aug. 2022.

[18] F. Yang, Y. Xie, and W. Cai, "The magnetic field analytical calculation in a novel double air-gaps permanent magnet Vernier synchronous motor," *IEEE Trans. Magn.*, vol. 57, no. 9, pp. 1–9, Sep. 2021.

[19] Z. Yu, Y. Li, Y. Jing, and J. Wang, "Cooling system of outer rotor SPMSM for a two-seater all-electric aircraft based on heat pipe technology," *IEEE Trans. Transport. Electrific.*, vol. 8, no. 2, pp. 1656–1664, Jun. 2022.

[20] S. Wu, D. Hao, and W. Tong, "Temperature field analysis of mine flameproof outer rotor permanent magnet synchronous motor with different cooling schemes," *CES Trans. Electr. Mach. Syst.*, vol. 6, no. 2, pp. 162–169, Jun. 2022.

[21] Q. Chen, H. Shao, J. Huang, H. Sun, and J. Xie, "Analysis of temperature field and water cooling of outer rotor in-wheel motor for electric vehicle," *IEEE Access*, vol. 7, pp. 140142–140151, 2019.

[22] W. Q. Chu and Z. Q. Zhu, "Investigation of torque ripples in permanent magnet synchronous machines with skewing," *IEEE Trans. Magn.*, vol. 49, no. 3, pp. 1211–1220, Mar. 2013.

[23] L. Li, G. Zhu, Y. Zhao, N. Jia, M. Xue, and Y. Li, "Design and analysis of different cooling schemes of a flux-modulated permanent magnet in-wheel motor for electric vehicle applications," *IET Electric Power Appl.*, vol. 15, no. 3, pp. 348–358, Mar. 2021.

[24] Y. Xu, B. Zhang, and G. Feng, "Electromagnetic design and thermal analysis of module combined permanent magnet motor with wrapped type for mine ball mill," *IET Electric Power Appl.*, vol. 16, no. 2, pp. 139–157, Feb. 2022.

[25] Y. Song, Y. Zhang, S. Jin, Z. Xu, and F. Zhang, "Investigation of winding cooling enhancement and thermal modelling of large-power high-torque-density direct-drive PMSM," *IET Electric Power Appl.*, early access, pp. 1–10, Aug. 2023, doi: 10.1049/elp2.12351.

SIYANG YU (Member, IEEE) received the B.S. and M.S. degrees in electrical engineering from the Shenyang University of Technology, Shenyang, China, in 2011 and 2014, respectively, the M.Sc. degree in mechatronics from Kyungsung University, Busan, South Korea, in 2014, and the Ph.D. degree in electrical engineering from the Shenyang University of Technology, in 2018. He is currently a Postdoctoral Researcher with the School of Electrical Engineering, Shenyang University of Technology. He has authored or coauthored more than 30 journals and conference papers. His research interests include design, analysis, and the control of electrical machines for industrial applications.

YONGDA SONG was born in Liaoning, China, in 1994. He received the B.S. degree in electrical engineering and automation from the Shenyang University of Technology, Shenyang, China, in 2017, where he is currently pursuing the Ph.D. degree in electrical engineering. His research interest includes the design and analysis of the low-speed high-torque PMSM.

GUANGWEI LIU (Member, IEEE) received the B.S., M.S., and Ph.D. degrees in electrical engineering from the Shenyang University of Technology, Shenyang, China, in 2005, 2008, and 2015, respectively. He is currently an Associate Professor in electrical machines with the School of Electrical Engineering, Shenyang University of Technology. His major research interests include permanent magnet electrical machines and its drive.

HAO WANG received the B.S., M.S., and Ph.D. degrees in electrical engineering from the Shenyang University of Technology, Shenyang, China, in 2014, 2017, and 2021, respectively. His research interests include dynamic modeling, simulations, and special machine electromagnetic design and wind power generation.

FENGGE ZHANG (Member, IEEE) received the B.S., M.S., and Ph.D. degrees in electrical engineering from the Shenyang University of Technology, Shenyang, China, in 1984, 1990, and 2000, respectively. Since 1984, he has been with the School of Electrical Engineering, Shenyang University of Technology, where he is currently a Professor. From October 2001 to July 2002, he was a Visiting Scholar with the Esslingen University of Applied Sciences, Esslingen, Germany. He has published numerous journals and conference papers on electrical machines and control systems. His research and teaching interests include electromagnetic theory, dynamic simulation, magnetic field analysis, optimized design, the computer control technology of electrical machines, and wind power generating systems.

● ● ●